PHOTONICS Research

AlGaN nanocrystals: building blocks for efficient ultraviolet optoelectronics

Xianhe Liu,[1,2] Kishwar Mashooq,[1] David A. Laleyan,[1] Eric T. Reid,[1] and Zetian Mi[1,*]

[1]Department of Electrical Engineering and Computer Science, University of Michigan, Ann Arbor, Michigan 48109, USA
[2]Department of Electrical and Computer Engineering, McGill University, Montreal, Quebec H3A 0E9, Canada
*Corresponding author: ztmi@umich.edu

Received 4 February 2019; revised 25 March 2019; accepted 1 April 2019; posted 1 April 2019 (Doc. ID 359506); published 17 May 2019

AlGaN nanocrystals have emerged as the building blocks of future optoelectronic devices operating in the ultraviolet (UV) spectral range. In this article, we describe the design and performance characteristics of AlGaN nanocrystal UV light-emitting diodes (LEDs) and surface-emitting UV laser diodes. The selective-area epitaxy and structural, optical, and electrical properties of AlGaN nanocrystals are presented. The recent experimental demonstrations of AlGaN nanocrystal LEDs and laser diodes are also discussed.

https://doi.org/10.1364/PRJ.7.000B12

1. INTRODUCTION

Ultraviolet (UV) light-emitting diodes (LEDs) and laser diodes are important for a broad range of applications, including water purification, disinfection, medical diagnostics, material processing, free-space optical communication, and atomic sensors [1–6]. High wall-plug efficiency, relatively high output power, and stable emission wavelengths are essential for these applications. In addition, UV laser diodes with very narrow spectral linewidths are critical for applications in high-performance atomic clocks and sensors [7,8]. In the past decade, significant progress has been made in UV optoelectronics with the use of AlGaN quantum wells [9–19]. External quantum efficiency (EQE) in the range of 10%–20% has been demonstrated in AlGaN quantum well LEDs operating at ~280 nm [12,16]. However, in a large part of the UV-C spectrum, the EQE of AlGaN quantum well LEDs remains extremely low (well below 1%) [17,20,21]. In addition, there have been no demonstrations of UV vertical cavity surface-emitting laser (VCSEL) diodes with the use of conventional AlGaN quantum wells [22]. The shortest wavelength for electrically pumped AlGaN quantum well edge-emitting lasers is limited to ~336 nm [23]. Some of the critical challenges for achieving high-performance AlGaN UV optoelectronic devices include the presence of large densities of defects and dislocations in the device active region due to the relatively large lattice mismatch (~2.5%) between AlN and GaN. Conventional planar AlGaN structures also exhibit extremely poor p-type conduction due to the very large activation energy of p-type (Mg) dopant (up to ~600 meV) and the formation of extensive compensating defects during epitaxy [24–26]. In addition, light polarization becomes predominantly transverse-magnetic (TM) polarized for Al-rich AlGaN [27], which prevents the realization of efficient light extraction for LEDs. The strong strain-induced polarization fields and the resulting quantum-confined Stark effect further decrease the device efficiency and the maximum achievable gain for laser diodes.

Recent studies suggest that AlGaN nanostructures hold immense promise to break the efficiency bottleneck of UV optoelectronics [28–38]. Due to the efficient surface strain relaxation, dislocation-free AlGaN nanostructures can be grown directly on foreign substrates including silicon, sapphire, and metals [29,39–48]. It has also been discovered that the formation energy for Al(Ga)-substitutional Mg dopant is significantly reduced in AlGaN nanostructures compared to their planar counterparts [42,49]. Room temperature hole concentration up to 6×10^{17} cm^{-3} has been measured in AlN nanostructures, which is nearly 7 orders of magnitude larger than that reported in AlN epilayers [25,49]. With the use of such AlGaN nanostructures, UV LEDs and laser diodes operating in the wavelength range of 210–340 nm have been demonstrated [28,31,35,42,50]. The challenge in forming metal contact on nanowires can be addressed by pendeo-epitaxy [36,51]. To date, such AlGaN nanostructures are generally formed spontaneously during epitaxy, which leads to large variations of size, spacing, and surface morphology. To realize high-performance UV optoelectronic devices, it is imperative to achieve AlGaN nanostructures and nanostructure arrays with precisely controlled properties. Such issues can be addressed with the use of the technique of selective-area epitaxy [33,36,52–58]. In this process, the formation of AlGaN nanostructures takes place on a nano-patterned substrate. As such, their size, spacing, and surface morphology can be predetermined and precisely controlled by the underlying nanoscale patterns. The alloy composition and therefore the emission wavelength can also be tuned through variations in the growth

conditions. Through the formation of core-shell heterostructures, detrimental effects such as surface recombination can be minimized or eliminated [33,59,60]. The resulting near-perfect AlGaN nanocrystals can therefore form the building blocks for next-generation UV optoelectronic devices.

Significantly, through the use of selective-area epitaxy, AlGaN nanocrystal arrays can form photonic crystal, or metamaterial structures with distinct properties and functionality. For example, by coupling in-plane emission to vertical emission, light-extraction efficiency (LEE) of AlGaN photonic crystal structures can, in principle, reach over 90% from the device top surface for TM-polarized photons, compared to <10% LEE for conventional planar quantum well devices [61]. In addition, surface-emitting UV lasers can be achieved by exploiting the two-dimensional band-edge resonant effect of an AlGaN photonic crystal [62–65]. At the band edge, the group velocity of light becomes zero, and a stable two-dimensional (2D) cavity mode (standing wave) is formed in the photonic crystal structure. The photonic crystal itself serves as a diffraction grating, and the output beam is emitted from the surface. Previously, an output power >1.5 W and a slope efficiency ~0.66 W/A have been achieved in an InGaAs photonic crystal surface-emitting laser operating at 941.5 nm under continuous-wave operation at room temperature [65]. However, there have been few studies on GaN photonic crystal surface-emitting lasers [66–68]. To date, the only reported electrically injected InGaN photonic crystal surface-emitting lasers have operated in the blue-violet spectral range ($\lambda \sim 406$ nm) with an extremely large threshold current density (~67 kA/cm^2) due to the large densities of defects in etched planar structures. Recently, with the use of nearly dislocation-free AlGaN nanocrystals, electrically injected photonic crystal lasers operating at ~369.6 nm have been demonstrated [69].

In this paper, we discuss the design, epitaxy, characterization, and emerging device applications of AlGaN nanocrystals. While nanocrystals may take different forms, our discussions are primarily focused on nanocrystals such as nanowires and nanorods. The design principle and theoretical performance of AlGaN nanocrystal UV LEDs and surface-emitting UV laser diodes are presented in Section 2. The epitaxy, structural, electronic, and optical properties of AlGaN nanocrystals are discussed in Section 3. In Section 4, we present recent demonstrations of AlGaN UV LEDs. The achievement of electrically pumped UV laser diodes with the use of AlGaN nanocrystals is presented in Section 5. Finally, conclusions are made in Section 6.

2. DESIGN OF AlGaN NANOCRYSTAL LEDS AND SURFACE-EMITTING LASER DIODES

The light extraction of conventional planar LED structures is often limited by total internal reflection. Such an issue can be potentially addressed by using photonic nanocrystal structures. For example, the incorporation of a periodic photonic crystal structure on the top or bottom of a planar LED structure can effectively couple the guided modes inside the device to radiative modes by diffraction [70–75]. With the use of this approach, a significant light-extraction efficiency (~73%) was demonstrated at ~450 nm [76]. A large periodic refractive index modulation can also be introduced inside an LED structure in the form of a nanowire array or two-dimensional photonic crystal slab. By engineering photonic band structure, e.g., inhibiting the guided mode using a photonic bandgap created by the periodic photonic crystal structure, light emitted from the device can only radiate to ambient medium, thereby leading to a high light-extraction efficiency [77]. The directionality of emitted light may also be controlled using this approach. A potential limitation of this approach, however, is that the internal quantum efficiency may be reduced due to the modification (reduction) of the photonic density of states and radiative recombination at the bandgap. An alternative approach is to enhance light extraction by Bragg scattering while increasing the photonic density of states [33,61,78,79]. In addition, photonic nanocrystals provide the distinct opportunity to engineer laser emission characteristics including threshold current, coupling coefficient, polarization, and far-field emission pattern [80–89].

A. Design of AlGaN Nanocrystal LEDs

One of the major causes for the extremely low EQE (below 1%) for AlGaN LEDs in a large part of the deep UV spectrum is the poor LEE. With Al content higher than 70%, photons are mostly emitted in the in-plane direction with TM polarization [27]. As a result, most photons are trapped and reabsorbed inside the device, which not only reduces the LEE but also leads to a severe heating effect. In this section, we discuss the use of photonic nanocrystals to enhance the LEE for such TM-polarized emission. The photonic nanocrystal structure consists of AlGaN nanocrystals with optimally designed lattice constant and size. Schematically shown in Fig. 1(a), the nanocrystal structure consists of n-Al(Ga)N, a n-AlGaN cladding layer, a AlGaN quantum well/dot active region, and a p-AlGaN layer. Figure 1(b) shows the top view of a photonic crystal structure and illustrates the definition of the lattice constant a and nanocrystal lateral size d. The photonic crystal

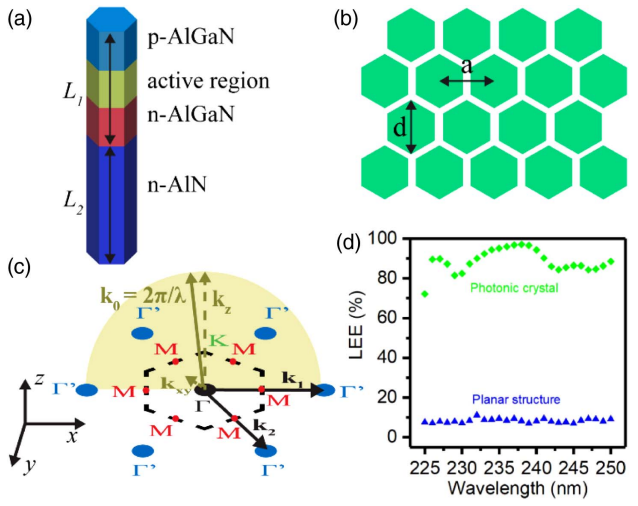

Fig. 1. (a) Schematic of an AlGaN nanocrystal. (b) Top view of a photonic crystal structure. (c) Schematic for the scattering process in the photonic crystal structure. (d) Light-extraction efficiency (LEE) for the planar structure and the photonic crystal structure with $a = 160$ nm and $d = 95$ nm [61].

structure described here is designed to have a Γ point at around 240 nm. At the Γ point, the in-plane wavevector k_{xy} is negligibly small, as shown in Fig. 1(c). The wavevector is therefore nearly perpendicular to the substrate, indicating that the in-plane emitted light is coupled to the vertical surface emission [90]. By employing UV-reflective substrates such as distributed Bragg reflectors, the light coupled downward can also be reflected and contribute to the device output from the top surface. Through detailed studies using finite-difference time-domain (FDTD) simulation, we have identified that the design with $a = 160$ nm and $d = 95$ nm can exhibit a very large LEE of >95%, which is due to the high out-of-plane coupling coefficient. Moreover, the LEE remains above 80% over a broad wavelength range. For comparison, the LEE of a conventional planar LED structure is also simulated, as shown in Fig. 1(d), which is less than 10%. The LEE is further calculated for practical device configurations that may incorporate a thin p-GaN layer and a thin narrow p-metal grid on top of the nanocrystals, which exhibit an LEE in the range of 30% to 40%. Therefore, the enhancement of LEE by using AlGaN nanocrystals is experimentally feasible.

B. Design of AlGaN Surface-Emitting Laser Diodes

We describe the design and performance characteristics of AlGaN nanocrystal band-edge lasers, which can exhibit surface emission but without the need of the thick and resistive distributed Bragg reflectors required for a conventional VCSEL [62–64,66,67]. By using slow light modes near the Γ point, wherein the in-plane wave vector is nearly zero, photonic crystal structures can be designed to emit light vertically and out of plane, i.e., from the top surface. While light output is designed to be in the vertical direction, there is also lateral leakage from the edge. These two paths of light emission largely determine the Q factor of the lasing mode. Given a certain photonic crystal design, the Q factors associated with vertical and lateral photon confinement generally increase with device area. The Q factors, however, also depend critically on the ratio of nanocrystal size to lattice constant. The maximum coupling to the vertical output and lateral leakage typically occurs at an intermediate ratio of nanocrystal size to lattice constant [91]. Because of the coupling in the vertical direction, some light is also coupled downward to the substrate. In this regard, the use of a reflective substrate/template can readily enhance the useful light output.

Illustrated in Fig. 2(a) (top left inset), AlGaN nanocrystals are arranged in a square lattice with a lattice constant a. AlGaN quantum dots/wells are incorporated in the nanocrystals to serve as the gain medium. Such nanocrystal arrays, with precisely controlled size and spacing, can be achieved using the technique of selective-area epitaxy to be described next [92–95]. To evaluate the device performance, we considered a laser structure consisting of 200 nm n- and p-$Al_{0.3}Ga_{0.7}N$ cladding layers and a 200 nm $Al_{0.09}Ga_{0.91}N$ guiding layer with the incorporation of five GaN (2 nm)/$Al_{0.09}Ga_{0.91}N$ (4 nm) quantum wells. Shown in Fig. 2(a), the photonic band structure was calculated by the finite-element method (FEM) simulation for nanocrystals with a lateral size of $0.35a$. The simulation was performed using the RF module of Comsol Multiphysics. The refractive index of AlGaN nanocrystals

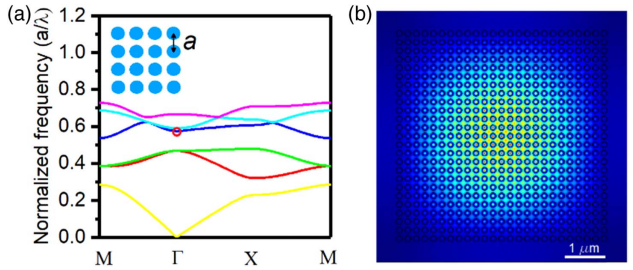

Fig. 2. (a) Photonic band structure of a photonic crystal with a lattice constant of 207 nm and a diameter of 144 nm. The inset is the top view showing the arrangement of nanocrystals. (b) The electric field distribution of the band-edge mode in the entire device.

is 2.65. The normalized frequency of the band-edge mode is 0.575 [shown as the red circle in Fig. 2(a)], which corresponds to $\lambda = 360$ nm for $a = 207$ nm. The group velocity is determined by the slope of the dispersion curve in the photonic band structure. At the band edge, the low group velocity is achieved when the slope of dispersion curve becomes zero ($d\omega/dk \to 0$), i.e., near the Γ point, the group velocity of light becomes zero, thereby leading to the formation of a stable and large single-cavity mode [96]. Moreover, the extremely low group velocity leads to the long interaction time between radiation field and active material and consequently gives rise to a strong gain enhancement. The intrinsic cavity quality factors are on the order of $(L/\lambda)^3$, where λ is the vacuum wavelength and $L \gg \lambda$ is the lateral dimension of the device structure [96]. Figure 2(b) shows the electric field profile of the band-edge mode calculated with the FEM method. By placing a single dipole source at the center of the simulated structure, the electric field spreads across the entire periodic nanocrystal array, which is a characteristic of the band-edge modes. In this study, photonic crystal arrays in a square region with lateral dimension L in the range of 2.5 to 10 μm are designed and investigated. The relatively large coherent lasing area can lead to excellent beam quality and is well suited for relatively high-output power operation.

1. Threshold Current Density

The performance of a photonic crystal surface-emitting laser can be estimated from a model based on standard rate equations for carriers and photons as follows:

$$\frac{dN}{dt} = \frac{J}{qd} - R_r - R_{nr} - N_{ph} g \frac{c}{n}, \tag{1}$$

$$\frac{dN_{ph}}{dt} = \Gamma_o N_{ph} g \frac{c}{n} - N_{ph} \alpha \frac{c}{n}. \tag{2}$$

The definitions of the parameters are listed in Table 1.

The threshold gain is given by

$$g_{th} = \alpha/\Gamma_o. \tag{3}$$

As the leakage of light at the edge of the device is usually designed to be much smaller than the vertical output, only the loss due to vertical output is considered for calculating the threshold current density. The loss is calculated from the Q factor extracted from 3D FDTD simulation using the relation

Table 1. Definition of Various Parameters Used in the Rate Equations

Parameter	Definition
N	Carrier concentration
N_{ph}	Photon density in the cavity
J	Current density
q	Electron charge
d	Total thickness of the active layers
R_r	Radiative recombination rate
R_{nr}	Nonradiative recombination rate
g	Material gain
c	Light speed in vacuum
n	Refractive index of the active layers
Γ_o	Optical confinement factor
α	Total loss

$$\alpha = \frac{2\pi}{aQ}. \tag{4}$$

The threshold gain is calculated for different device dimensions, and then the threshold current is calculated based on the charge carrier recombination in the active region. Since recombination mostly occurs in the quantum well, any recombination in the bulk region was not taken into account. The nonradiative recombination rate can be written as $R_{nr} = AN + CN^3$, where A is the Shockley–Read–Hall recombination coefficient and C is the Auger recombination coefficient. To estimate the threshold current, Auger recombination is neglected due to the large bandgap, and A is assumed to be 3×10^8 s^{-1} [97,98]. The radiative recombination rate R_r at a certain carrier concentration is calculated by integrating the recombination rate over the entire energy distribution of carriers [99]. The optical confinement factor is estimated to be 1.6% from the FEM simulation. The threshold current density is shown in Fig. 3(a). It is seen that the threshold current density decreases drastically with increasing lasing area due to the higher Q. For a lateral size of 10 μm × 10 μm, the threshold current density is ~4.9 kA/cm^2 at room temperature. Much smaller threshold current density is expected for devices with a larger Q factor. In practice, the laser threshold depends critically on the design of the active region and the device fabrication process.

2. Lasing Linewidth

Semiconductor lasers with narrow linewidths are very important for emerging quantum applications, including atomic clocks and sensors. To date, the narrowest linewidth of VCSELs is ~3 MHz, which was realized by using a very long cavity and by minimizing the mirror loss [100,101]. Such a linewidth, however, is approximately 2 to 3 orders of magnitude larger than the best reported values for distributed feedback (DFB) lasers or distributed Bragg reflector lasers [102,103]. In the spectral range from UV to green, the linewidth of typical diode lasers is on the order of 100 GHz or larger [104–108].

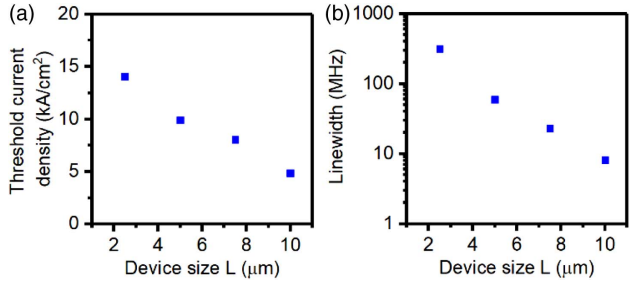

Fig. 3. Variation of (a) threshold current density and (b) linewidth at an injection current of $5 \times I_{th}$ with the device lateral dimension (L).

Linewidths of a semiconductor laser are often affected by the Q factor of the cavity mode, output power, and linewidth enhancement factor [7]. The linewidth of a laser can be approximately estimated by [109]

$$\Delta\nu = \frac{R_{sp}(1 + f_\alpha^2)}{4\pi N_{ph} V_m}, \tag{5}$$

where R_{sp} is the rate of spontaneous emission into the lasing mode, f_α is the linewidth enhancement factor, and V_m is the mode volume. The photon number is written as [110]

$$N_{ph} V_m = \frac{1}{\exp[(\hbar\omega - \Delta E_F)/kT] - 1}, \tag{6}$$

where $\hbar\omega$ is the photon energy, ΔE_F is the difference between quasi-Fermi levels, k is the Boltzmann constant, and T is the temperature. The rate of spontaneous emission into the lasing mode is [110]

$$R_{sp} = \alpha v_g \exp[(\Delta E_F - \hbar\omega)/kT], \tag{7}$$

where v_g is the group velocity. Considering the definitions for α, v_g, and Q, we have

$$\alpha = -\frac{dN_{ph}}{N_{ph} dx}, \tag{8}$$

$$v_g = dx/dt, \tag{9}$$

$$Q = -\frac{dN_{ph}}{N_{ph} dt}. \tag{10}$$

Combining Eqs. (7)–(10), the rate of spontaneous emission into the lasing mode can be written as

$$R_{sp} = \frac{\omega}{Q[1 + (N_{ph} V_m)^{-1}]}. \tag{11}$$

Because the photon number is typically much larger than one above threshold, the rate of spontaneous emission into the lasing mode is approximately given by

$$R_{sp} \approx \omega/Q. \tag{12}$$

Above threshold current I_{th}, the photon number at an injection current I can then be expressed as

$$N_{ph} V_m = \frac{\tau_{ph}}{q}(I - I_{th}), \tag{13}$$

where the photon lifetime τ_{ph} can be calculated by

$$\tau_{ph} = Q/\omega. \tag{14}$$

Based on the analysis above, the linewidth can be written as

$$\Delta\nu = \frac{\omega^2(1 + f_\alpha^2)}{4\pi Q^2 q(I - I_{th})}. \tag{15}$$

In this study, the linewidth was calculated at a current density of $5 \times I_{th}$ for photonic crystal lasers with different lateral dimensions (up to 10 μm) as shown in Fig. 3(b). A typical linewidth enhancement factor of 2 was used in the calculation [111]. It is seen that the linewidth decreases drastically with increasing device size. This is explained by the larger photon number in the lasing mode and higher Q associated with larger device dimensions. For a photonic nanocrystal surface-emitting laser diode with a lateral dimension ~10 μm, the linewidth is ~8 MHz, which is 5 to 6 orders smaller than that of previously reported GaN-based VCSELs in the UV–visible spectrum and is on the same order of magnitude of the narrowest linewidths reported for VCSELs operating in the infrared spectrum [100,101,104–108]. The narrowest linewidth of laser diodes reported to date is ~3.6 kHz, which was measured from a DFB laser [103]. It is expected that the linewidth of photonic crystal surface-emitting laser diodes can be potentially reduced to ~kilohertz (kHz) by increasing the device size and further optimizing the design.

3. Far-Field Pattern and Mode Profile

Illustrated in Fig. 4 is the simulated far-field pattern using the FDTD method for a photonic crystal structure with a lattice constant of 207 nm and a diameter of 144 nm, showing predominantly a narrow, single-lobed beam due to the coherent oscillation over a large area. Nearly ideal beam quality ($M^2 < 1.1$) and high-output power operation (up to 3.5 W) were achieved previously in InGaAs photonic crystal band-edge lasers operating at 940 nm at room temperature [65]. For the presented photonic nanocrystal surface-emitting laser diodes, by varying the lattice points and/or lattice phases, it is also possible to tune the beam shape and realize surface-emitting laser diodes with on-demand beam characteristics [79,80].

3. EPITAXY AND CHARACTERISTICS OF AlGaN NANOCRYSTALS

Previous studies on the epitaxy of AlGaN nanostructures have been largely focused on spontaneously formed nanowire arrays by using metalorganic vapour-phase epitaxy, or molecular beam epitaxy [29,39–46], which often exhibit random distribution in size, height, and morphology and twist/tilt in crystal orientation [36]. The resultant Al distribution is highly

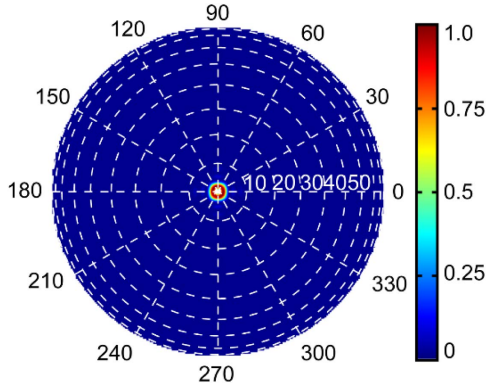

Fig. 4. Far-field radiation pattern calculated for a photonic nanocrystal laser structure with a lattice constant of 207 nm and a diameter of 144 nm.

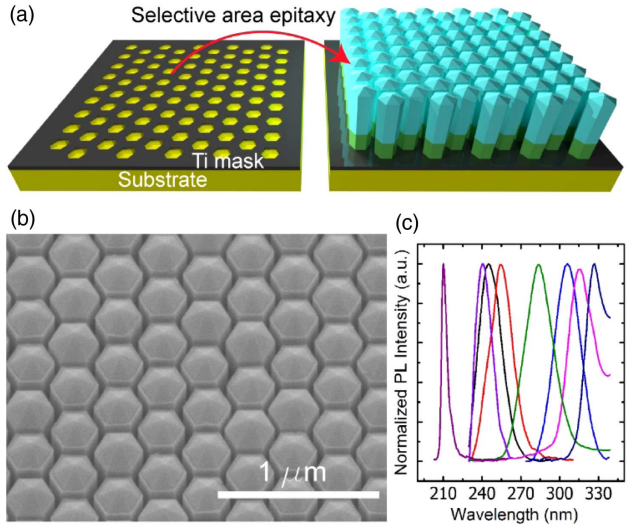

Fig. 5. (a) Schematic of the selective-area epitaxy process. (b) A typical SEM image of AlGaN nanocrystals grown by selective-area epitaxy. (c) Normalized PL spectra for AlGaN nanocrystals with Al content across nearly the entire compositional range [33].

non-uniform, leading to relatively large inhomogeneous broadening [28,29]. In addition, the coalescence of nanowires with misaligned crystal orientation can lead to the formation of extensive defects and dislocations [36]. These issues can be largely addressed by using the technique of selective-area epitaxy [52,53], which can yield AlGaN nanocrystals with precisely controlled size, position, and surface polarity. This growth process is schematically shown in Fig. 5(a). A thin Ti (or SiN_x) layer is first deposited on the substrate surface and patterned by electron beam lithography. Nitridation of the Ti mask is performed at 400°C to prevent Ti cracking during growth [52,55]. GaN (or AlN) nanocrystal array is grown under a relatively high temperature to achieve high growth selectivity. AlGaN is subsequently grown on the GaN (or AlN) nanocrystals. Shown in Fig. 5(b) is the typical scanning electron microscopy (SEM) image of AlGaN nanocrystal array grown by plasma-assisted molecular beam epitaxy (MBE). The Al incorporation can be varied across the entire compositional range by changing the Al beam equivalent pressure during epitaxy [33,112]. Shown in Fig. 5(c) are the photoluminescence (PL) spectra of AlGaN nanocrystals with Al compositions of ~20% to 80% measured at room temperature.

Due to the efficient surface strain relaxation, dislocation-free AlGaN nanocrystals can be grown on foreign substrates. Shown in Fig. 6(a) is ~0.5 μm GaN epilayer grown directly on Si(001), which exhibits large densities of pits and dislocations. In contrast, N-polar GaN nanocrystals grown on such GaN/Si templates exhibit smooth surface morphology and are relatively free of pits and dislocations, due to the termination of propagating dislocations on the lateral surfaces of nanocrystals [36]. Moreover, through controlled coalescence process of AlGaN nanocrystals, nearly dislocation-free AlGaN templates can be achieved on sapphire or other foreign substrates [36]. With the incorporation of Mg dopant, the coalesced $Al_{0.35}Ga_{0.65}N$ epilayers can exhibit excellent p-type conduction characteristics,

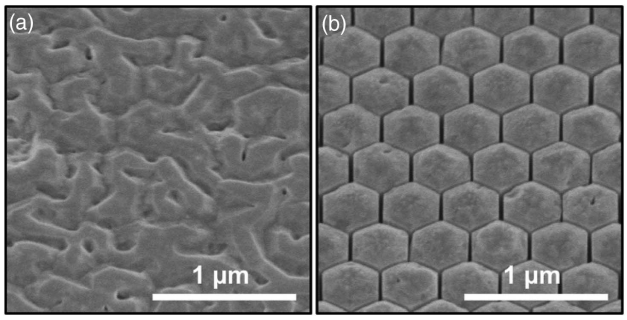

Fig. 6. SEM images of (a) 0.5 μm GaN grown on Si wafer and (b) N-polar GaN nanocrystals grown on Si.

including a free-hole concentration of $\sim 7 \times 10^{18}$ cm^{-3} and mobility ~ 8.85 $cm^2/(V \cdot s)$ at room temperature, which are significantly better than previously reported values, respectively [113–115]. High-performance UV LEDs have also been demonstrated with the use of such AlGaN templates [36]. Significantly, the surface polarity can be controllably tuned to be N-polar, Ga(Al)-polar, or semi-polar when grown on foreign substrates [116–118]. The capacity to realize dislocation-free AlGaN nanostructures and heterostructures with controlled surface polarity provides a distinct opportunity to significantly enhance the performance of mid- and deep-UV optoelectronic and high-power/frequency electronic devices [33,34,36,42,43,45,119–121].

Dislocation-free AlGaN nanocrystals also offer unique advantages for achieving efficient p-type conduction that was difficult for conventional AlGaN epilayers. Shown in Fig. 7(a) are the photoluminescence emission spectra for Mg-doped AlN nanostructures measured at room temperature. The photoluminescence emission of a non-doped sample is also shown for comparison. The pronounced peak at ~230 nm corresponds to a Mg-acceptor related transition, which is separated from the excitonic emission of AlN by ~0.5–0.6 eV, in good agreement with previous report for the activation energy for Mg-acceptor level in AlN [122]. Experimentally, we have measured a very small activation energy (~20–50 meV near room temperature) for Mg dopant in AlN nanostructures at high Mg-doping concentrations [49,123]. The hole concentration can reach up to 6×10^{17} cm^{-3} at room temperature, which is nearly 7 orders of magnitude larger than that of previously reported AlN epilayers [25,49]. Such unusually large carrier concentration is directly related to hole hopping conduction in the Mg

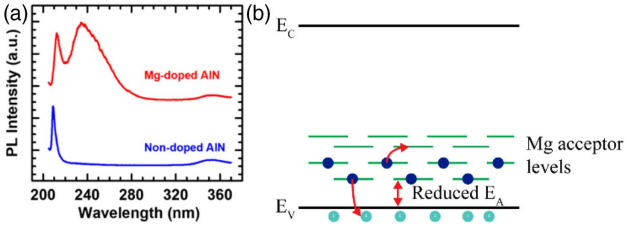

Fig. 7. (a) PL emission spectra of AlN and AlN:Mg nanostructures measured at room temperature. (b) Schematic illustration of the Mg impurity band of AlN nanostructures due to high Mg concentration and the reduced activation energy for a portion of Mg acceptors.

impurity band of AlN nanocrystals. Recent first-principle calculations have shown that Al(Ga) substitutional Mg formation energy is significantly reduced in nanocrystals compared to their planar counterparts [42,124], which can lead to enhanced Mg-dopant incorporation without the formation of extensive defects. The resulting large concentrations of Mg acceptors in Al(Ga)N lead to several critical benefits for efficient p-type conduction. (i) The high Mg acceptor concentration promotes the formation of a Mg impurity band in Al(Ga)N nanocrystals due to the strong interaction of neighboring dopants, which can lead to efficient hole hopping conduction in the impurity band. The two-band conduction model is schematically shown in Fig. 7(b). (ii) In addition, a portion of the Mg dopants have much reduced ionization energy and can be readily ionized and contribute to free holes in valence band due to the band-tailing effect and the broadened Mg energy level distribution, which is evidenced by the partial overlap between the photoluminescence emission of Mg acceptors and the excitonic transition of AlN, as shown in Fig. 7(a). The formation of an impurity band in doped semiconductors has also been reported and analyzed previously [5,42,49,114,125,126]. Also, during the epitaxy of AlGaN nanocrystals, the growth conditions can be tuned to be N-rich, which makes the formation of N-vacancy-related defects energetically less favorable than metal-rich condition [127]. Furthermore, the luminescence related to such N vacancies was also shown to be absent under N-rich conditions by Shahedipour *et al.*, suggesting the formation of N-vacancy-related defects is suppressed [128]. It is therefore evident that the use of dislocation-free nanocrystals can provide a viable path to achieve efficient p-type conduction in ultra-wide-bandgap AlGaN that was previously difficult.

4. AlGaN NANOCRYSTAL UV LEDS

In this section, we review some recent progress on AlGaN nanocrystal UV LEDs. Due to the enhanced p-type conduction, AlN nanostructured LEDs exhibit excellent current-voltage characteristics. It was demonstrated that these devices could exhibit a turn-on voltage ~6–7 V, which is much better than that of conventional planar AlN LEDs [25,37,129]. Recently, hexagonal boron nitride (h-BN) was incorporated into AlN LED structures, which led to a significant improvement in device performance [130]. h-BN has been demonstrated to have much higher p-type conductivity than Mg-doped AlN [130]. Recent theoretical calculations showed that certain type of point defects, e.g., boron vacancies, could behave like acceptors [131–133]. In a recent study, h-BN was used to replace conventional p-AlN layer in an AlN LED, shown in the inset of Fig. 8(a). After the growth of AlN nanocrystals, the growth of h-BN was performed at substrate temperatures from 400 to 800°C in a separate MBE system where boron was *in situ* evaporated by electron beam. The growth of BN was conducted under N-rich conditions to promote the formation of boron vacancies, which served as shallow p-type acceptors. The device exhibits excellent current-voltage characteristics with a turn-on voltage of 5.5 V and negligible leakage current under reverse bias. In contrast, the turn-on voltage for conventional AlN epilayer LEDs is larger than 20 V [25]. The electroluminescence (EL) spectra measured under different injection currents at room

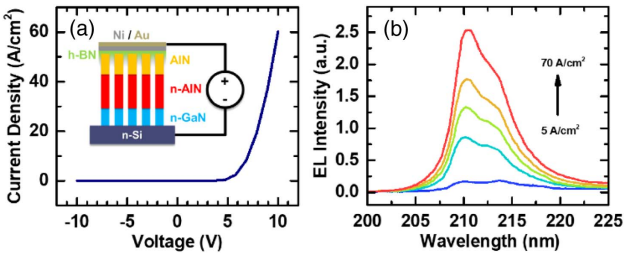

Fig. 8. (a) *I-V* characteristics of a 300 μm × 300 μm LED device at room temperature. Inset: schematic of the fabricated LED structure. (b) Room temperature EL spectra of the LED device for various injection currents [35].

temperature are shown in Fig. 8(b). The main electroluminescence peak is at 210 nm, which is from exciton emission. The presence of a shoulder on the longer wavelength side of the emission spectra is attributed to longitudinal optical phonon replica [134]. The measured light output is more than one order higher than a similar AlN nanowire LED but without the use of h-BN. The improved performance is attributed to more efficient hole transport and injection and better carrier confinement in the active region.

Tunnel injection of nonequilibrium holes has shown to be effective in improving hole injection efficiency and recombination in the active region [32,135–139]. An n^{++}-GaN/Al/p^{++}-AlGaN tunnel junction was incorporated in AlGaN UV LEDs to improve the hole injection. The EL spectra under different injection currents are shown in Fig. 9(a). A single pronounced peak at 275 nm is measured. Compared to LEDs without a tunnel junction, a drastic improvement in the output power (by nearly 2 orders of magnitude) was measured, as shown in Fig. 9(b). With the use of AlGaN nanostructures, LEDs operating at 240 nm have also been demonstrated with improved performance [140].

5. AlGaN NANOCRYSTAL UV LASER DIODES

Described in Section 2.B, AlGaN nanocrystals offer a distinct opportunity to realize low-threshold UV laser diodes. The first demonstrations of electrically pumped semiconductor laser diodes operating in the UV-B and UV-C bands were realized

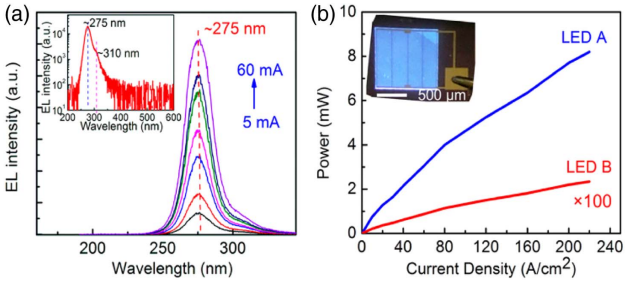

Fig. 9. (a) EL spectra of the Al tunnel junction AlGaN UV LED under CW biasing condition. Inset: EL spectrum in the logarithmic scale. (b) Variations of output power with injection current for Al tunnel junction AlGaN UV LED and standard p-i-n AlGaN UV LED. Inset: an optical image of the device under an injection current of 8 A/cm² [31].

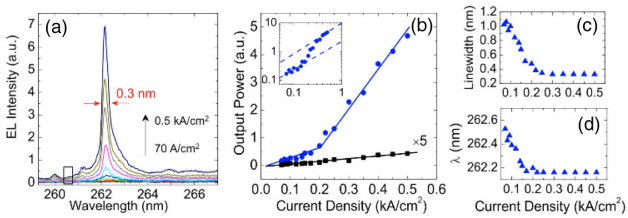

Fig. 10. (a) Emission spectra for an AlGaN laser operating at 262 nm at 77 K under various injection current densities. (b) Variation of output with injection current. Blue circles represent the lasing peak. Black squares represent the background emission in the boxed area in (a) with a linewidth of 0.3 nm. The inset plots the data for the lasing peak in the logarithmic scale. Variations of (c) linewidth and (d) peak wavelength of the lasing peak at 262 nm with injection current density [30].

using AlGaN nanostructures [29,34,141,142]. Such subwavelength nanostructures can form a high-*Q* optical cavity due to Anderson localization of light [34,143–147]. Shown in Fig. 10(a) are the electroluminescence spectra of a laser diode based on Anderson localization in spontaneously formed AlGaN nanostructures [29]. A sharp and pronounced lasing peak at 262 nm is measured at 77 K. Variations of the light output versus injection current are displayed in Fig. 10(b), showing a threshold current density ~200 A/cm², which is nearly 2 orders lower than recently reported AlGaN quantum well laser diodes at 336 nm and 342 nm [23,148]. The logarithmic plot of the light intensity versus current density is shown in the inset of Fig. 10(b), which exhibits a clear S-shaped trend, further confirming the achievement of lasing. Compared to the lasing emission, the background emission [black squares in Fig. 10(b)] exhibits a small or negligible increase above threshold. The spectral linewidth and the peak wavelength of the lasing mode are plotted in Figs. 10(c) and 10(d), respectively. A significant reduction of the linewidth to ~0.3 nm was measured at the threshold current density ~200 A/cm², providing unambiguous evidence for the achievement of lasing. Above threshold, the lasing emission peak stays nearly constant at 262.2 nm.

More recently, we have demonstrated an AlGaN laser diode operating at 239 nm at room temperature [142]. Numerical simulation is performed to identify the average diameters and filling factors that can support high-*Q* random cavity modes around 240 nm. The growth of nanocrystals is optimized for the suited average diameters and filling factors, and the Al content is increased accordingly to tune the emission wavelength to around 240 nm. The emission spectra measured under various injection currents are shown in Fig. 11(a), which are characterized by broad spontaneous emission below threshold and a sharp lasing peak above threshold. Variations of the light output for the lasing mode versus injection current are shown in Fig. 11(b), which exhibits a distinct threshold current ~0.35 mA. The light intensity versus injection current exhibits a clear S shape when plotted in a logarithmic scale, shown in the inset of Fig. 11(b), further confirming the achievement of lasing. For comparison, the background emission around 267 nm indicated by the black box in Fig. 11(a) was also analyzed,

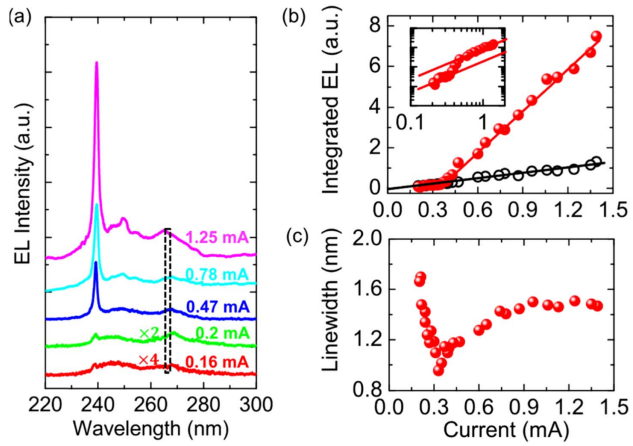

Fig. 11. (a) Emission spectra of an AlGaN laser device operating at 239 nm in CW biasing condition under different injection currents. (b) Variation of output with injection current for the lasing peak (red filled circles) and a non-lasing cavity mode (black open circles) from the boxed region in (a). The inset plots the data for the lasing peak in the logarithmic scale. (c) Variations of linewidth with the injection current [142].

which only exhibited a very small increase with current above threshold [black circles in Fig. 11(b)]. Variations of the spectral linewidth of the lasing peak versus injection current are shown in Fig. 11(c). A clear reduction of the linewidth is seen at threshold.

6. CONCLUSION

In summary, dislocation-free AlGaN nanocrystals hold tremendous promise to break the efficiency bottleneck of UV optoelectronics. With the use of selective-area epitaxy by MBE, their structural, electronic, and optical properties can be controlled. Through photonic band gap engineering, AlGaN nanocrystal LEDs promise significantly improved light-extraction efficiency for TM-polarized photons. AlGaN nanocrystals also provide a viable path to achieve electrically pumped semiconductor lasers in the UV-B and UV-C bands, including both edge- and surface-emitting devices with superior performance. The current challenges include the development of UV-transparent electrode and passivation materials, which are essentially required to achieve efficient AlGaN nanocrystal LEDs and laser didoes in the mid- and deep-UV spectra.

Funding. Army Research Office (ARO) (W911NF-17-1-0109); National Science Foundation (NSF) (DMR-1807984). Competing Interest: intellectual property related to this work has been licensed to NS Nanotech Inc., which was founded by Z. Mi.

REFERENCES

1. P. S. Ramanujam and R. H. Berg, "Photodimerization in dipeptides for high capacity optical digital storage," Appl. Phys. Lett. **85**, 1665–1667 (2004).
2. M. Würtele, T. Kolbe, M. Lipsz, A. Külberg, M. Weyers, M. Kneissl, and M. Jekel, "Application of GaN-based ultraviolet-C light emitting diodes-UV LEDs-for water disinfection," Water Res. **45**, 1481–1489 (2011).
3. K. G. Lindenauer and J. L. Darby, "Ultraviolet disinfection of wastewater: effect of dose on subsequent photoreactivation," Water Res. **28**, 805–817 (1994).
4. B. W. Chwirot, S. Chwirot, W. Jedrzejczyk, M. Jackowski, A. M. Raczyńska, J. Winczakiewicz, and J. Dobber, "Ultraviolet laser-induced fluorescence of human stomach tissues: detection of cancer tissues by imaging techniques," Lasers Surg. Med. **21**, 149–158 (1997).
5. P. D. D. Schwindt, Y. Jau, H. L. Partner, D. K. Serkland, A. Ison, A. McCants, E. Winrow, J. Prestage, J. Kellogg, N. Yu, C. D. Boschen, I. Kosvin, D. Mailloux, D. Scherer, C. Nelson, A. Hati, and D. A. Howe, "Miniature trapped-ion frequency standard with $^{171}Yb^{+}$," in *Joint Conference of the IEEE International Frequency Control Symposium & the European Frequency and Time Forum* (IEEE, 2015), pp. 752–757.
6. J. D. Robert and M. S. Brian, "Survey of ultraviolet non-line-of-sight communications," Semicond. Sci. Technol. **29**, 084006 (2014).
7. D. K. Serkland, G. A. Keeler, K. M. Geib, and G. M. Peake, "Narrow linewidth VCSELs for high-resolution spectroscopy," Proc. SPIE **7229**, 722907 (2009).
8. S. Olmschenk, D. Hayes, D. N. Matsukevich, P. Maunz, D. L. Moehring, K. C. Younge, and C. Monroe, "Measurement of the lifetime of the 6p $^2P^o_{1/2}$ level of Yb^+," Phys. Rev. A **80**, 022502 (2009).
9. H. Hirayama, N. Noguchi, T. Yatabe, and N. Kamata, "227 nm AlGaN light-emitting diode with 0.15 mW output power realized using a thin quantum well and AlN buffer with reduced threading dislocation density," Appl. Phys. Express **1**, 051101 (2008).
10. H. Hirayama, N. Noguchi, and N. Kamata, "222 nm deep-ultraviolet AlGaN quantum well light-emitting diode with vertical emission properties," Appl. Phys. Express **3**, 032102 (2010).
11. M. Jo, N. Maeda, and H. Hirayama, "Enhanced light extraction in 260 nm light-emitting diode with a highly transparent p-AlGaN layer," Appl. Phys. Express **9**, 012102 (2015).
12. M. Shatalov, W. Sun, A. Lunev, X. Hu, A. Dobrinsky, Y. Bilenko, J. Yang, M. Shur, R. Gaska, C. Moe, G. Garrett, and M. Wraback, "AlGaN deep-ultraviolet light-emitting diodes with external quantum efficiency above 10%," Appl. Phys. Express **5**, 082101 (2012).
13. J. R. Grandusky, J. Chen, S. R. Gibb, M. C. Mendrick, C. G. Moe, L. Rodak, G. A. Garrett, M. Wraback, and L. J. Schowalter, "270 nm pseudomorphic ultraviolet light-emitting diodes with over 60 mW continuous wave output power," Appl. Phys. Express **6**, 032101 (2013).
14. A. Fujioka, K. Asada, H. Yamada, T. Ohtsuka, T. Ogawa, T. Kosugi, D. Kishikawa, and T. Mukai, "High-output-power 255/280/310 nm deep ultraviolet light-emitting diodes and their lifetime characteristics," Semicond. Sci. Technol. **29**, 084005 (2014).
15. C. Pernot, S. Fukahori, T. Inazu, T. Fujita, M. Kim, Y. Nagasawa, A. Hirano, M. Ippommatsu, M. Iwaya, S. Kamiyama, I. Akasaki, and H. Amano, "Development of high efficiency 255–355 nm AlGaN-based light-emitting diodes," Phys. Status Solidi A **208**, 1594–1596 (2011).
16. T. Takano, T. Mino, J. Sakai, N. Noguchi, K. Tsubaki, and H. Hirayama, "Deep-ultraviolet light-emitting diodes with external quantum efficiency higher than 20% at 275 nm achieved by improving light-extraction efficiency," Appl. Phys. Express **10**, 031002 (2017).
17. T. Kolbe, F. Mehnke, M. Guttmann, C. Kuhn, J. Rass, T. Wernicke, and M. Kneissl, "Improved injection efficiency in 290 nm light emitting diodes with Al(Ga)N electron blocking heterostructure," Appl. Phys. Lett. **103**, 031109 (2013).
18. F. Mehnke, C. Kuhn, M. Guttmann, C. Reich, T. Kolbe, V. Kueller, A. Knauer, M. Lapeyrade, S. Einfeldt, J. Rass, T. Wernicke, M. Weyers, and M. Kneissl, "Efficient charge carrier injection into sub-250 nm AlGaN multiple quantum well light emitting diodes," Appl. Phys. Lett. **105**, 051113 (2014).
19. M. Kneissl, T. Kolbe, C. Chua, V. Kueller, N. Lobo, J. Stellmach, A. Knauer, H. Rodriguez, S. Einfeldt, Z. Yang, N. M. Johnson, and M. Weyers, "Advances in group III-nitride-based deep UV light-emitting diode technology," Semicond. Sci. Technol. **26**, 014036 (2010).

20. H. Hirayama, S. Fujikawa, N. Noguchi, J. Norimatsu, T. Takano, K. Tsubaki, and N. Kamata, "222–282 nm AlGaN and InAlGaN-based deep-UV LEDs fabricated on high-quality AlN on sapphire," Phys. Status Solidi A **206**, 1176–1182 (2009).
21. H. Hirayama, T. Yatabe, N. Noguchi, T. Ohashi, and N. Kamata, "226-273 nm AlGaN deep-ultraviolet light-emitting diodes fabricated on multilayer AlN buffers on sapphire," Phys. Status Solidi C **5**, 2969–2971 (2008).
22. H.-C. Yu, Z.-W. Zheng, Y. Mei, R.-B. Xu, J.-P. Liu, H. Yang, B.-P. Zhang, T.-C. Lu, and H.-C. Kuo, "Progress and prospects of GaN-based VCSEL from near UV to green emission," Prog. Quantum Electron. **57**, 1–19 (2018).
23. H. Yoshida, Y. Yamashita, M. Kuwabara, and H. Kan, "Demonstration of an ultraviolet 336 nm AlGaN multiple-quantum-well laser diode," Appl. Phys. Lett. **93**, 241106 (2008).
24. M. L. Nakarmi, N. Nepal, C. Ugolini, T. M. Altahtamouni, J. Y. Lin, and H. X. Jiang, "Correlation between optical and electrical properties of Mg-doped AlN epilayers," Appl. Phys. Lett. **89**, 152120 (2006).
25. Y. Taniyasu, M. Kasu, and T. Makimoto, "An aluminium nitride light-emitting diode with a wavelength of 210 nanometres," Nature **441**, 325–328 (2006).
26. U. Kaufmann, P. Schlotter, H. Obloh, K. Köhler, and M. Maier, "Hole conductivity and compensation in epitaxial GaN:Mg layers," Phys. Rev. B **62**, 10867–10872 (2000).
27. H. Kawanishi, M. Senuma, M. Yamamoto, E. Niikura, and T. Nukui, "Extremely weak surface emission from (0001) *c*-plane AlGaN multiple quantum well structure in deep-ultraviolet spectral region," Appl. Phys. Lett. **89**, 081121 (2006).
28. S. Zhao, S. Y. Woo, S. M. Sadaf, Y. Wu, A. Pofelski, D. A. Laleyan, R. T. Rashid, Y. Wang, G. A. Botton, and Z. Mi, "Molecular beam epitaxy growth of Al-rich AlGaN nanowires for deep ultraviolet optoelectronics," APL Mater. **4**, 086115 (2016).
29. S. Zhao, S. Y. Woo, M. Bugnet, X. Liu, J. Kang, G. A. Botton, and Z. Mi, "Three-dimensional quantum confinement of charge carriers in self-organized AlGaN nanowires: a viable route to electrically injected deep ultraviolet lasers," Nano Lett. **15**, 7801–7807 (2015).
30. S. Zhao, X. Liu, S. Y. Woo, J. Kang, G. A. Botton, and Z. Mi, "An electrically injected AlGaN nanowire laser operating in the ultraviolet-C band," Appl. Phys. Lett. **107**, 043101 (2015).
31. S. M. Sadaf, S. Zhao, Y. Wu, Y. H. Ra, X. Liu, S. Vanka, and Z. Mi, "An AlGaN core-shell tunnel junction nanowire light-emitting diode operating in the ultraviolet-C band," Nano Lett. **17**, 1212–1218 (2017).
32. S. M. Sadaf, Y. H. Ra, T. Szkopek, and Z. Mi, "Monolithically integrated metal/semiconductor tunnel junction nanowire light-emitting diodes," Nano Lett. **16**, 1076–1080 (2016).
33. X. Liu, B. H. Le, S. Y. Woo, S. Zhao, A. Pofelski, G. A. Botton, and Z. Mi, "Selective area epitaxy of AlGaN nanowire arrays across nearly the entire compositional range for deep ultraviolet photonics," Opt. Express **25**, 30494–30502 (2017).
34. K. H. Li, X. Liu, Q. Wang, S. Zhao, and Z. Mi, "Ultralow-threshold electrically injected AlGaN nanowire ultraviolet lasers on Si operating at low temperature," Nat. Nanotechnol. **10**, 140–144 (2015).
35. D. A. Laleyan, S. Zhao, S. Y. Woo, H. N. Tran, H. B. Le, T. Szkopek, H. Guo, G. A. Botton, and Z. Mi, "AlN/h-BN heterostructures for Mg dopant-free deep ultraviolet photonics," Nano Lett. **17**, 3738–3743 (2017).
36. B. H. Le, S. Zhao, X. Liu, S. Y. Woo, G. A. Botton, and Z. Mi, "Controlled coalescence of AlGaN nanowire arrays: an architecture for nearly dislocation-free planar ultraviolet photonic device applications," Adv. Mater. **28**, 8446–8454 (2016).
37. X. Liu, S. Zhao, B. H. Le, and Z. Mi, "Molecular beam epitaxial growth and characterization of AlN nanowall deep UV light emitting diodes," Appl. Phys. Lett. **111**, 101103 (2017).
38. S. Zhao, H. P. T. Nguyen, M. G. Kibria, and Z. Mi, "III-Nitride nanowire optoelectronics," Prog. Quantum Electron. **44**, 14–68 (2015).
39. S. P. Young, B. R. Hwang, J. C. Lee, I. Hyunsik, H. Y. Cho, T. W. Kang, J. H. Na, and C. M. Park, "Self-assembled $Al_xGa_{1-x}N$ nanorods grown on Si(001) substrates by using plasma-assisted molecular beam epitaxy," Nanotechnology **17**, 4640–4643 (2006).
40. J. Ristić, M. A. Sánchez-García, E. Calleja, J. Sanchez-Páramo, J. M. Calleja, U. Jahn, and K. H. Ploog, "AlGaN nanocolumns grown by molecular beam epitaxy: optical and structural characterization," Phys. Status Solidi A **192**, 60–66 (2002).
41. K. A. Bertness, A. Roshko, N. A. Sanford, J. M. Barker, and A. V. Davydov, "Spontaneously grown GaN and AlGaN nanowires," J. Cryst. Growth **287**, 522–527 (2006).
42. S. Zhao, A. T. Connie, M. H. Dastjerdi, X. H. Kong, Q. Wang, M. Djavid, S. Sadaf, X. D. Liu, I. Shih, H. Guo, and Z. Mi, "Aluminum nitride nanowire light emitting diodes: breaking the fundamental bottleneck of deep ultraviolet light sources," Sci. Rep. **5**, 8332 (2015).
43. F. K. Thomas, D. C. Santino, A. T. M. Sarwar, J. P. Patrick, F. K. Robert, and C. M. Roberto, "Deep ultraviolet emitting polarization induced nanowire light emitting diodes with $Al_xGa_{1-x}N$ active regions," Nanotechnology **25**, 455201 (2014).
44. S. D. Carnevale, T. F. Kent, P. J. Phillips, A. T. M. G. Sarwar, C. Selcu, R. F. Klie, and R. C. Myers, "Mixed polarity in polarization-induced p-n junction nanowire light-emitting diodes," Nano Lett. **13**, 3029–3035 (2013).
45. A. Pierret, C. Bougerol, S. Murcia-Mascaros, A. Cros, H. Renevier, B. Gayral, and B. Daudin, "Growth, structural and optical properties of AlGaN nanowires in the whole composition range," Nanotechnology **24**, 115704 (2013).
46. A. Pierret, C. Bougerol, M. D. Hertog, B. Gayral, M. Kociak, H. Renevier, and B. Daudin, "Structural and optical properties of $Al_xGa_{1-x}N$ nanowires," Phys. Status Solidi (RRL) **7**, 868–873 (2013).
47. Y. Wu, Y. Wang, K. Sun, and Z. Mi, "Molecular beam epitaxy and characterization of AlGaN nanowire ultraviolet light emitting diodes on Al coated Si (001) substrate," J. Cryst. Growth **507**, 65–69 (2019).
48. B. Janjua, H. Sun, C. Zhao, D. H. Anjum, D. Priante, A. A. Alhamoud, F. Wu, X. Li, A. M. Albadri, A. Y. Alyamani, M. M. El-Desouki, T. K. Ng, and B. S. Ooi, "Droop-free $Al_xGa_{1-x}N/Al_yGa_{1-y}N$ quantum-disks-in-nanowires ultraviolet LED emitting at 337 nm on metal/silicon substrates," Opt. Express **25**, 1381–1390 (2017).
49. N. H. Tran, B. H. Le, S. Zhao, and Z. Mi, "On the mechanism of highly efficient p-type conduction of Mg-doped ultra-wide-bandgap AlN nanostructures," Appl. Phys. Lett. **110**, 032102 (2017).
50. Q. Wang, A. T. Connie, H. P. Nguyen, M. G. Kibria, S. Zhao, S. Sharif, I. Shih, and Z. Mi, "Highly efficient, spectrally pure 340 nm ultraviolet emission from $Al_xGa_{1-x}N$ nanowire based light emitting diodes," Nanotechnology **24**, 345201 (2013).
51. B. Janjua, H. Sun, C. Zhao, D. H. Anjum, F. Wu, A. A. Alhamoud, X. Li, A. M. Albadri, A. Y. Alyamani, M. M. El-Desouki, T. K. Ng, and B. S. Ooi, "Self-planarized quantum-disks-in-nanowires ultraviolet-B emitters utilizing pendeo-epitaxy," Nanoscale **9**, 7805–7813 (2017).
52. K. Kishino, H. Sekiguchi, and A. Kikuchi, "Improved Ti-mask selective-area growth (SAG) by rf-plasma-assisted molecular beam epitaxy demonstrating extremely uniform GaN nanocolumn arrays," J. Cryst. Growth **311**, 2063–2068 (2009).
53. T. Schumann, T. Gotschke, F. Limbach, T. Stoica, and R. Calarco, "Selective-area catalyst-free MBE growth of GaN nanowires using a patterned oxide layer," Nanotechnology **22**, 095603 (2011).
54. K. Tomioka, K. Ikejiri, T. Tanaka, J. Motohisa, S. Hara, K. Hiruma, and T. Fukui, "Selective-area growth of III-V nanowires and their applications," J. Mater. Res. **26**, 2127–2141 (2011).
55. A. Bengoechea-Encabo, F. Barbagini, S. Fernández-Garrido, J. Grandal, J. Ristic, M. A. Sanchez-Garcia, E. Calleja, U. Jahn, E. Luna, and A. Trampert, "Understanding the selective area growth of GaN nanocolumns by MBE using Ti nanomasks," J. Cryst. Growth **325**, 89–92 (2011).
56. H. J. Chu, T. W. Yeh, L. Stewart, and P. D. Dapkus, "Wurtzite InP nanowire arrays grown by selective area MOCVD," Phys. Status Solidi C **7**, 2494–2497 (2010).
57. H. Paetzelt, V. Gottschalch, J. Bauer, G. Benndorf, and G. Wagner, "Selective-area growth of GaAs and InAs nanowires—homo- and heteroepitaxy using templates," J. Cryst. Growth **310**, 5093–5097 (2008).
58. J. Motohisa, J. Noborisaka, J. Takeda, M. Inari, and T. Fukui, "Catalyst-free selective-area MOVPE of semiconductor nanowires

on (111)B oriented substrates," J. Cryst. Growth **272**, 180–185 (2004).
59. R. Wang, X. Liu, I. Shih, and Z. Mi, "High efficiency, full-color AlInGaN quaternary nanowire light emitting diodes with spontaneous core-shell structures on Si," Appl. Phys. Lett. **106**, 261104 (2015).
60. Q. Wang, H. P. T. Nguyen, K. Cui, and Z. Mi, "High efficiency ultraviolet emission from $Al_xGa_{1-x}N$ core-shell nanowire heterostructures grown on Si (111) by molecular beam epitaxy," Appl. Phys. Lett. **101**, 043115 (2012).
61. X. Liu, K. Mashooq, T. Szkopek, and Z. Mi, "Improving the efficiency of transverse magnetic polarized emission from AlGaN based LEDs by using nanowire photonic crystal," IEEE Photon. J. **10**, 4501211 (2018).
62. J. D. Joannopoulos, S. G. Johnson, J. N. Winn, and R. D. Meade, *Photonic Crystals: Molding the Flow of Light* (Princeton University, 2011).
63. K. Busch, S. Lölkes, R. B. Wehrspohn, and H. Föll, *Photonic Crystals* (Wiley, 2004).
64. T. F. Krauss, "Photonic crystals for integrated optics," in *AIP Conference Proceedings* (IOP Publishing, 2001), pp. 89–98.
65. K. Hirose, Y. Liang, Y. Kurosaka, A. Watanabe, T. Sugiyama, and S. Noda, "Watt-class high-power, high-beam-quality photonic-crystal lasers," Nat. Photonics **8**, 406–411 (2014).
66. T. Kouno, K. Kishino, K. Yamano, and A. Kikuchi, "Two-dimensional light confinement in periodic InGaN/GaN nanocolumn arrays and optically pumped blue stimulated emission," Opt. Express **17**, 20440–20447 (2009).
67. J. B. Wright, S. Liu, G. T. Wang, Q. Li, A. Benz, D. D. Koleske, P. Lu, H. Xu, L. Lester, T. S. Luk, I. Brener, and G. Subramania, "Multi-colour nanowire photonic crystal laser pixels," Sci. Rep. **3**, 2982 (2013).
68. H. Matsubara, S. Yoshimoto, H. Saito, Y. Jianglin, Y. Tanaka, and S. Noda, "GaN photonic-crystal surface-emitting laser at blue-violet wavelengths," Science **319**, 445–447 (2008).
69. B. H. Le, X. Liu, N. H. Tran, S. Zhao, and Z. Mi, "An electrically injected AlGaN nanowire defect-free photonic crystal ultraviolet laser," Opt. Express **27**, 5843–5850 (2019).
70. M. Charlton, M. Zoorob, and T. Lee, "Photonic quasi-crystal LEDs: design, modelling, and optimisation," Proc. SPIE **6486**, 64860R (2007).
71. A. A. Erchak, D. J. Ripin, S. Fan, P. Rakich, J. D. Joannopoulos, E. P. Ippen, G. S. Petrich, and L. A. Kolodziejski, "Enhanced coupling to vertical radiation using a two-dimensional photonic crystal in a semiconductor light-emitting diode," Appl. Phys. Lett. **78**, 563–565 (2001).
72. A. David, B. Moran, K. McGroddy, E. Matioli, E. L. Hu, S. P. DenBaars, S. Nakamura, and C. Weisbuch, "GaN/InGaN light emitting diodes with embedded photonic crystal obtained by lateral epitaxial overgrowth," Appl. Phys. Lett. **92**, 113514 (2008).
73. C. Wiesmann, K. Bergenek, N. Linder, and U. Schwarz, "Analysis of the emission characteristics of photonic crystal LEDs," Proc. SPIE **6989**, 69890L (2008).
74. H. Benisty, J. Danglot, A. Talneau, S. Enoch, J. M. Pottage, and A. David, "Investigation of extracting photonic crystal lattices for guided modes of GaAs-based heterostructures," IEEE J. Quantum Electron. **44**, 777–789 (2008).
75. C.-Y. Cho, J.-B. Lee, S.-J. Lee, S.-H. Han, T.-Y. Park, J. W. Kim, Y. C. Kim, and S.-J. Park, "Improvement of light output power of InGaN/GaN light-emitting diode by lateral epitaxial overgrowth using pyramidal-shaped SiO_2," Opt. Express **18**, 1462–1468 (2010).
76. J. J. Wierer, Jr., A. David, and M. M. Megens, "III-nitride photonic-crystal light-emitting diodes with high extraction efficiency," Nat. Photonics **3**, 163–169 (2009).
77. M. Fujita, S. Takahashi, Y. Tanaka, T. Asano, and S. Noda, "Simultaneous inhibition and redistribution of spontaneous light emission in photonic crystals," Science **308**, 1296–1298 (2005).
78. M. Boroditsky, R. Vrijen, R. Coccioli, R. Bhat, and E. Yablonovitch, "Spontaneous emission extraction and Purcell enhancement from thin-film 2-D photonic crystals," J. Lightwave Technol. **17**, 2096–2112 (1999).
79. S. Noda, M. Yokoyama, M. Imada, A. Chutinan, and M. Mochizuki, "Polarization mode control of two-dimensional photonic crystal laser by unit cell structure design," Science **293**, 1123–1125 (2001).
80. S. Iwahashi, Y. Kurosaka, K. Sakai, K. Kitamura, N. Takayama, and S. Noda, "Higher-order vector beams produced by photonic-crystal lasers," Opt. Express **19**, 11963–11968 (2011).
81. Y. Liang, C. Peng, K. Sakai, S. Iwahashi, and S. Noda, "Three-dimensional coupled-wave model for square-lattice photonic crystal lasers with transverse electric polarization: a general approach," Phys. Rev. B **84**, 195119 (2011).
82. Y. Liang, C. Peng, K. Ishizaki, S. Iwahashi, K. Sakai, Y. Tanaka, K. Kitamura, and S. Noda, "Three-dimensional coupled-wave analysis for triangular-lattice photonic-crystal surface-emitting lasers with transverse-electric polarization," Opt. Express **21**, 565–580 (2013).
83. E. Miyai and S. Noda, "Phase-shift effect on a two-dimensional surface-emitting photonic-crystal laser," Appl. Phys. Lett. **86**, 111113 (2005).
84. N. Yokouchi, A. J. Danner, and K. D. Choquette, "Vertical-cavity surface-emitting laser operating with photonic crystal seven-point defect structure," Appl. Phys. Lett. **82**, 3608–3610 (2003).
85. K. Nozaki and T. Baba, "Laser characteristics with ultimate-small modal volume in photonic crystal slab point-shift nanolasers," Appl. Phys. Lett. **88**, 211101 (2006).
86. T. Baba, D. Sano, K. Nozaki, K. Inoshita, Y. Kuroki, and F. Koyama, "Observation of fast spontaneous emission decay in GaInAsP photonic crystal point defect nanocavity at room temperature," Appl. Phys. Lett. **85**, 3989–3991 (2004).
87. W. R. Frei, H. Johnson, and K. D. Choquette, "Optimization of a single defect photonic crystal laser cavity," J. Appl. Phys. **103**, 033102 (2008).
88. H. Altug, D. Englund, and J. Vučković, "Ultrafast photonic crystal nanocavity laser," Nat. Phys. **2**, 484–488 (2006).
89. C. Wiesmann, K. Bergenek, N. Linder, and U. T. Schwarz, "Photonic crystal LEDs-designing light extraction," Laser Photon. Rev. **3**, 262–286 (2009).
90. M. Imada, A. Chutinan, S. Noda, and M. Mochizuki, "Multidirectionally distributed feedback photonic crystal lasers," Phys. Rev. B **65**, 195306 (2002).
91. R. J. E. Taylor, D. M. Williams, J. R. Orchard, D. T. D. Childs, S. Khamas, and R. A. Hogg, "Band structure and waveguide modelling of epitaxially regrown photonic crystal surface-emitting lasers," J. Phys. D **46**, 264005 (2013).
92. Y.-T. Lin, T.-W. Yeh, Y. Nakajima, and P. D. Dapkus, "Catalyst-free GaN nanorods synthesized by selective area growth," Adv. Funct. Mater. **24**, 3162–3171 (2014).
93. T. F. Kuech and L. J. Mawst, "Nanofabrication of III-V semiconductors employing diblock copolymer lithography," J. Phys. D **43**, 183001 (2010).
94. S. D. Hersee, X. Sun, and X. Wang, "The controlled growth of GaN nanowires," Nano Lett. **6**, 1808–1811 (2006).
95. A. K. Rishinaramangalam, S. M. Ul Masabih, M. N. Fairchild, J. B. Wright, D. M. Shima, G. Balakrishnan, I. Brener, S. R. J. Brueck, and D. F. Feezell, "Controlled growth of ordered III-nitride core-shell nanostructure arrays for visible optoelectronic devices," J. Electron. Mater. **44**, 1255–1262 (2014).
96. R. Merlin and S. Young, "Photonic crystals as topological high-*Q* resonators," Opt. Express **22**, 18579–18587 (2014).
97. H. Yoshida, M. Kuwabara, Y. Yamashita, K. Uchiyama, and H. Kan, "Radiative and nonradiative recombination in an ultraviolet GaN/AlGaN multiple-quantum-well laser diode," Appl. Phys. Lett. **96**, 211122 (2010).
98. C. E. Dreyer, A. Alkauskas, J. L. Lyons, J. S. Speck, and C. G. V. D. Walle, "Gallium vacancy complexes as a cause of Shockley-Read-Hall recombination in III-nitride light emitters," Appl. Phys. Lett. **108**, 141101 (2016).
99. S. L. Chuang, *Physics of Photonic Devices* (Wiley, 2009).
100. F. M. D. Sopra, H. P. Zappe, M. Moser, R. Hovel, H. Gauggel, and K. Gulden, "Near-infrared vertical-cavity surface-emitting lasers with 3-MHz linewidth," IEEE Photon. Technol. Lett. **11**, 1533–1535 (1999).
101. P. Signoret, F. Marin, S. Viciani, G. Belleville, M. Myara, J. P. Tourrenc, B. Orsal, A. Plais, F. Gaborit, and J. Jacquet, "3.6-MHz linewidth 1.55-μm monomode vertical-cavity surface-emitting laser," IEEE Photon. Technol. Lett. **13**, 269–271 (2001).

102. R. M. Lammert, J. S. Hughes, S. D. Roh, M. L. Osowski, A. M. Jones, and J. J. Coleman, "Low-threshold narrow-linewidth InGaAs-GaAs ridge-waveguide DBR lasers with first-order surface gratings," IEEE Photon. Technol. Lett. **9**, 149–151 (1997).
103. M. Okai, M. Suzuki, and T. Taniwatari, "Strained multiquantum-well corrugation-pitch-modulated distributed feedback laser with ultranarrow (3.6 kHz) spectral linewidth," Electron. Lett. **29**, 1696–1697 (1993).
104. W.-J. Liu, X.-L. Hu, L.-Y. Ying, J.-Y. Zhang, and B.-P. Zhang, "Room temperature continuous wave lasing of electrically injected GaN-based vertical cavity surface emitting lasers," Appl. Phys. Lett. **104**, 251116 (2014).
105. M. Kuramoto, S. Kobayashi, T. Akagi, K. Tazawa, K. Tanaka, T. Saito, and T. Takeuchi, "High-output-power and high-temperature operation of blue GaN-based vertical-cavity surface-emitting laser," Appl. Phys. Express **11**, 112101 (2018).
106. Y.-S. Liu, A. F. M. Saniul Haq, K. Mehta, T.-T. Kao, S. Wang, H. Xie, S.-C. Shen, P. D. Yoder, F. A. Ponce, T. Detchprohm, and R. D. Dupuis, "Optically pumped vertical-cavity surface-emitting laser at 374.9 nm with an electrically conducting n-type distributed Bragg reflector," Appl. Phys. Express **9**, 111002 (2016).
107. G. Weng, Y. Mei, J. Liu, W. Hofmann, L. Ying, J. Zhang, Y. Bu, Z. Li, H. Yang, and B. Zhang, "Low threshold continuous-wave lasing of yellow-green InGaN-QD vertical-cavity surface-emitting lasers," Opt. Express **24**, 15546–15553 (2016).
108. K. Ikeyama, Y. Kozuka, K. Matsui, S. Yoshida, T. Akagi, Y. Akatsuka, N. Koide, T. Takeuchi, S. Kamiyama, M. Iwaya, and I. Akasaki, "Room-temperature continuous-wave operation of GaN-based vertical-cavity surface-emitting lasers with n-type conducting AlInN/GaN distributed Bragg reflectors," Appl. Phys. Express **9**, 102101 (2016).
109. C. Henry, "Theory of the linewidth of semiconductor lasers," IEEE J. Quantum Electron. **18**, 259–264 (1982).
110. C. H. Henry, R. A. Logan, and F. R. Merritt, "Measurement of gain and absorption spectra in AlGaAs buried heterostructure lasers," J. Appl. Phys. **51**, 3042–3050 (1980).
111. S. H. Park and S. L. Chuang, "Linewidth enhancement factor of wurtzite GaN/AlGaN quantum-well lasers with spontaneous polarization and piezoelectric effects," Appl. Phys. A **78**, 107–111 (2004).
112. K. Yamano, K. Kishino, H. Sekiguchi, T. Oto, A. Wakahara, and Y. Kawakami, "Novel selective area growth (SAG) method for regularly arranged AlGaN nanocolumns using nanotemplates," J. Cryst. Growth **425**, 316–321 (2015).
113. M. L. Nakarmi, K. H. Kim, M. Khizar, Z. Y. Fan, J. Y. Lin, and H. X. Jiang, "Electrical and optical properties of Mg-doped $Al_{0.7}Ga_{0.3}N$ alloys," Appl. Phys. Lett. **86**, 092108 (2005).
114. T. Kinoshita, T. Obata, H. Yanagi, and S.-I. Inoue, "High p-type conduction in high-Al content Mg-doped AlGaN," Appl. Phys. Lett. **102**, 012105 (2013).
115. M. L. Nakarmi, K. H. Kim, J. Li, J. Y. Lin, and H. X. Jiang, "Enhanced p-type conduction in GaN and AlGaN by Mg-δ-doping," Appl. Phys. Lett. **82**, 3041–3043 (2003).
116. K. Hestroffer, C. Leclere, C. Bougerol, H. Renevier, and B. Daudin, "Polarity of GaN nanowires grown by plasma-assisted molecular beam epitaxy on Si(111)," Phys. Rev. B **84**, 245302 (2011).
117. A. Urban, J. Malindretos, J. H. Klein-Wiele, P. Simon, and A. Rizzi, "Ga-polar GaN nanocolumn arrays with semipolar faceted tips," New J. Phys. **15**, 053045 (2013).
118. M. D. Brubaker, S. M. Duff, T. E. Harvey, P. T. Blanchard, A. Roshko, A. W. Sanders, N. A. Sanford, and K. A. Bertness, "Polarity-controlled GaN/AlN nucleation layers for selective-area growth of GaN nanowire arrays on Si(111) substrates by molecular beam epitaxy," Cryst. Growth Des. **16**, 596–604 (2016).
119. S. Wienecke, B. Romanczyk, M. Guidry, H. Li, X. Zheng, E. Ahmadi, K. Hestroffer, L. Megalini, S. Keller, and U. K. Mishra, "N-polar deep recess MISHEMTs with record 2.9 W/mm at 94 GHz," IEEE Electron. Dev. Lett. **37**, 713–716 (2016).
120. S. Wienecke, B. Romanczyk, M. Guidry, H. Li, E. Ahmadi, K. Hestroffer, X. Zheng, S. Keller, and U. K. Mishra, "N-polar GaN cap MISHEMT with record power density exceeding 6.5 W/mm at 94 GHz," IEEE Electron. Dev. Lett. **38**, 359–362 (2017).
121. B. Romanczyk, S. Wienecke, M. Guidry, H. Li, E. Ahmadi, X. Zheng, S. Keller, and U. K. Mishra, "Demonstration of constant 8 W/mm power density at 10, 30, and 94 GHz in state-of-the-art millimeter-wave N-polar GaN MISHEMTs," IEEE Trans. Electron. Devices **65**, 45–50 (2018).
122. M. L. Nakarmi, N. Nepal, J. Y. Lin, and H. X. Jiang, "Photoluminescence studies of impurity transitions in Mg-doped AlGaN alloys," Appl. Phys. Lett. **94**, 091903 (2009).
123. A. T. Connie, S. Zhao, S. M. Sadaf, I. Shih, Z. Mi, X. Du, J. Lin, and H. Jiang, "Optical and electrical properties of Mg-doped AlN nanowires grown by molecular beam epitaxy," Appl. Phys. Lett. **106**, 213105 (2015).
124. S. Zhao, B. H. Le, D. P. Liu, X. D. Liu, M. G. Kibria, T. Szkopek, H. Guo, and Z. Mi, "p-Type InN nanowires," Nano Lett. **13**, 5509–5513 (2013).
125. A. A. Allerman, M. H. Crawford, M. A. Miller, and S. R. Lee, "Growth and characterization of Mg-doped AlGaN-AlN short-period superlattices for deep-UV optoelectronic devices," J. Cryst. Growth **312**, 756–761 (2010).
126. P. Kozodoy, M. Hansen, S. P. DenBaars, and U. K. Mishra, "Enhanced Mg doping efficiency in $Al_{0.2}Ga_{0.8}N$/GaN superlattices," Appl. Phys. Lett. **74**, 3681–3683 (1999).
127. K. Laaksonen, M. G. Ganchenkova, and R. M. Nieminen, "Vacancies in wurtzite GaN and AlN," J. Phys. Condens. Matter **21**, 015803 (2008).
128. F. Shahedipour and B. W. Wessels, "Investigation of the formation of the 2.8 eV luminescence band in p-type GaN:Mg," Appl. Phys. Lett. **76**, 3011–3013 (2000).
129. S. Zhao, M. Djavid, and Z. Mi, "Surface emitting, high efficiency near-vacuum ultraviolet light source with aluminum nitride nanowires monolithically grown on silicon," Nano Lett. **15**, 7006–7009 (2015).
130. R. Dahal, J. Li, S. Majety, B. N. Pantha, X. K. Cao, J. Y. Lin, and H. X. Jiang, "Epitaxially grown semiconducting hexagonal boron nitride as a deep ultraviolet photonic material," Appl. Phys. Lett. **98**, 211110 (2011).
131. C. Attaccalite, M. Bockstedte, A. Marini, A. Rubio, and L. Wirtz, "Coupling of excitons and defect states in boron-nitride nanostructures," Phys. Rev. B **83**, 144115 (2011).
132. W. Orellana and H. Chacham, "Stability of native defects in hexagonal and cubic boron nitride," Phys. Rev. B **63**, 125205 (2001).
133. V. Wang, R. J. Liu, H. P. He, C. M. Yang, and L. Ma, "Hybrid functional with semi-empirical van der Waals study of native defects in hexagonal BN," Solid State Commun. **177**, 74–79 (2014).
134. Y. Taniyasu and M. Kasu, "Origin of exciton emissions from an AlN p-n junction light-emitting diode," Appl. Phys. Lett. **98**, 131910 (2011).
135. Z. Yuewei, A. A. Andrew, K. Sriram, A. Fatih, W. M. Michael, M. A. Andrew, and R. Siddharth, "Enhanced light extraction in tunnel junction-enabled top emitting UV LEDs," Appl. Phys. Express **9**, 052102 (2016).
136. Y. Zhang, S. Krishnamoorthy, J. M. Johnson, F. Akyol, A. Allerman, M. W. Moseley, A. Armstrong, J. Hwang, and S. Rajan, "Interband tunneling for hole injection in III-nitride ultraviolet emitters," Appl. Phys. Lett. **106**, 141103 (2015).
137. S. M. Sadaf, Y. H. Ra, H. P. T. Nguyen, M. Djavid, and Z. Mi, "Alternating-current InGaN/GaN tunnel junction nanowire white-light emitting diodes," Nano Lett. **15**, 6696–6701 (2015).
138. A. T. M. G. Sarwar, B. J. May, J. I. Deitz, T. J. Grassman, D. W. McComb, and R. C. Myers, "Tunnel junction enhanced nanowire ultraviolet light emitting diodes," Appl. Phys. Lett. **107**, 101103 (2015).
139. Y. Zhang, S. Krishnamoorthy, F. Akyol, A. A. Allerman, M. W. Moseley, A. M. Armstrong, and S. Rajan, "Design and demonstration of ultra-wide bandgap AlGaN tunnel junctions," Appl. Phys. Lett. **109**, 121102 (2016).
140. S. Zhao, S. M. Sadaf, S. Vanka, Y. Wang, R. Rashid, and Z. Mi, "Sub-milliwatt AlGaN nanowire tunnel junction deep ultraviolet light emitting diodes on silicon operating at 242 nm," Appl. Phys. Lett. **109**, 201106 (2016).
141. B. H. Le, S. Zhao, N. H. Tran, T. Szkopek, and Z. Mi, "On the Fermi-level pinning of InN grown surfaces," Appl. Phys. Express **8**, 061001 (2015).
142. S. Zhao, X. Liu, Y. Wu, and Z. Mi, "An electrically pumped 239 nm AlGaN nanowire laser operating at room temperature," Appl. Phys. Lett. **109**, 191106 (2016).

143. M. Sakai, Y. Inose, K. Ema, T. Ohtsuki, H. Sekiguchi, A. Kikuchi, and K. Kishino, "Random laser action in GaN nanocolumns," Appl. Phys. Lett. **97**, 151109 (2010).
144. M.-H. Lo, Y.-J. Cheng, M.-C. Liu, H.-C. Kuo, and S. C. Wang, "Lasing at exciton transition in optically pumped gallium nitride nanopillars," Opt. Express **19**, 17960–17965 (2011).
145. C. Y. Liu, H. Y. Xu, J. G. Ma, X. H. Li, X. T. Zhang, Y. C. Liu, and R. Mu, "Electrically pumped near-ultraviolet lasing from ZnO/MgO core/shell nanowires," Appl. Phys. Lett. **99**, 063115 (2011).
146. S. F. Yu, C. Yuen, S. P. Lau, W. I. Park, and G.-C. Yi, "Random laser action in ZnO nanorod arrays embedded in ZnO epilayers," Appl. Phys. Lett. **84**, 3241–3243 (2004).
147. J. Liu, P. D. Garcia, S. Ek, N. Gregersen, T. Suhr, M. Schubert, J. Mørk, S. Stobbe, and P. Lodahl, "Random nanolasing in the Anderson localized regime," Nat. Nanotechnol. **9**, 285–289 (2014).
148. H. Yoshida, Y. Yamashita, M. Kuwabara, and H. Kan, "A 342-nm ultraviolet AlGaN multiple-quantum-well laser diode," Nat. Photonics **2**, 551–554 (2008).